https://doi.org/10.1016/j.apenergy.2019.113406

Bifunctional electrocatalytic activity of $La_{0.8}Sr_{0.2}MnO_3$-based perovskite with the A-site deficiency for oxygen reduction and evolution reactions in alkaline media

Rong-hua Yuan[a], Yun He[a], Wei He[b], Meng Ni[b], Michael K. H. Leung[a]*

[a] Ability R&D Energy Research Centre, School of Energy and Environment, City University of Hong Kong, Hong Kong, China.

[b] Building Energy Research Group, Department of Building and Real Estate, The Hong Kong Polytechnic University, Hong Kong, China

*Corresponding authors:

E-mail: mkh.leung@cityu.edu.hk (*Michael K. H. Leung*)

Abstract

The development of efficient noble-metal free electrocatalysts for oxygen reduction reaction (ORR) and oxygen evolution reaction (OER) is of great importance for energy storage devices, such as fuel cell and zinc-air battery. In this work, we report a facile approach to enhance the electrocatalytic activity of $La_{0.8}Sr_{0.2}MnO_3$-based perovskite by introducing the deficiency in the A-site and transition-metal Fe in the B-site. Bifunctional electrocatalysts $La_{0.8}Sr_{0.2}MnO_3$,

The short version of the paper was presented at ICAE2018, Aug 22-25, Hong Kong. This paper is a substantial extension of the short version of the conference paper.

$(La_{0.8}Sr_{0.2})_{0.98}MnO_3$, $(La_{0.8}Sr_{0.2})_{0.95}MnO_3$ and $(La_{0.8}Sr_{0.2})_{0.95}Mn_{0.5}Fe_{0.5}O_3$ were prepared by a facile sol-gel process. The material characterization results showed that compared with $La_{0.8}Sr_{0.2}MnO_3$, $(La_{0.8}Sr_{0.2})_{0.98}MnO_3$ and $(La_{0.8}Sr_{0.2})_{0.95}MnO_3$ have smaller particle size, more oxygen vacancies and proper Mn valence, which will benefit both ORR and OER. The results were verified by testing the electrocatalytic activities using rotating-disk electrode (RDE) in alkaline media. For the perovskite oxides with only A-site cation deficiency, the bifunctional electrocatalytic activities increase in the following order: $La_{0.8}Sr_{0.2}MnO_3$ < $(La_{0.8}Sr_{0.2})_{0.98}MnO_3$ < $(La_{0.8}Sr_{0.2})_{0.95}MnO_3$. With partial substitution of Mn by Fe in the B-site, the $(La_{0.8}Sr_{0.2})_{0.95}Mn_{0.5}Fe_{0.5}O_3$ perovskite oxide exhibits even better electrocatalytic activity. Further experiments reveal that $(La_{0.8}Sr_{0.2})_{0.95}Mn_{0.5}Fe_{0.5}O_3$ has the highest current density (4.5 mA cm^{-2}) in ORR which is comparable to commercial Pt/C (5 mA cm^{-2}) and the enhancement of the OER is more obvious than that of the ORR. Subsequently, the perovskite samples were used as the cathode catalysts in zinc-air batteries. The results further prove that proper use of A-site deficiency and B-site Fe doping in perovskite oxides can boost up the electrocatalytic activities.

Keywords: Perovskite; Oxygen reduction reaction; Oxygen evolution reaction; A-site deficiency; Zinc-air battery.

The short version of the paper was presented at ICAE2018, Aug 22-25, Hong Kong. This paper is a substantial extension of the short version of the conference paper.

1. Introduction

With the growing demand for clean and renewable energy, substantial attention has been paid to the technologies of energy storage and conversion [1-3]. Promising solutions include rechargeable metal-air batteries and fuel cells [4-6]. The development of rechargeable metal-air batteries and fuel cells is largely limited by two sluggish mechanisms, namely, oxygen reduction reaction (ORR) and oxygen evolution reaction (OER) kinetics of the oxygen catalysts [7-10]. Presently, Pt and IrO_2 are commonly chosen as benchmarks for ORR and OER, respectively. However, the noble metal catalysts are not suitable for practical applications such as zinc-air battery, as they suffer the problems of the limited availability, unsatisfactory durability, high cost and uni-functionality [11-13]. Therefore, present research emphasizes the development of noble-metal free electrocatalysts for improving performance and lowering cost [14, 15].

Until now, many types of noble metal-free catalysts, for example, the transition metal oxides in form of perovskites, spinels, and their dopant, have been reported [16-19]. Among various bifunctional catalysts, perovskite-based oxides usually have the universal formula ABO_3, where A and B represents the alkaline-earth (or rare-earth) metals and transition metals, respectively. The perovskite-based oxides

The short version of the paper was presented at ICAE2018, Aug 22-25, Hong Kong. This paper is a substantial extension of the short version of the conference paper.

have been applied as oxygen catalyst for the reason of their exciting catalytic activity and stability in alkaline solution [20-23]. One attractive feature of the perovskite is that we can easily control the properties of the perovskite oxides by partially substituting the A- or B-site cations and hence generate the corresponding oxides with desired structures, oxygen contents, and the most important electrocatalytic properties [24-27]. Among perovskite oxides, $LaMnO_3$, which is a typical perovskite, has a variety of applications, such as gas sensors, oxygen catalysts and solid oxide fuel cells[28-30]. However, when used as a catalyst, $LaMnO_3$ exhibits insufficient ORR and OER activities in alkaline solution. Thus, the main objective is to enhance the ORR and OER.

Kuai et al. reported a mesoporous $LaMnO_{3+delta}$ perovskite for ORR with remarkable activity synthesized by a facile aerosol-spray assisted approach [31]. Zhao et al. demonstrated that the strontium-doped perovskite oxide $La_{0.4}Sr_{0.6}MnO_3$ is a highly efficient electrocatalyst for nonaqueous Li-O_2 battery [32]. Hu et al. confirmed that doping Ca into the $LaMnO_3$ composites could tune their catalytic activity as catalyst in zinc-air battery [33]. Apart from the doping method, creating the A-site deficiency has been reported to be an effective approach to improve the electrochemical ability of perovskite catalysts [34-36]. Recently, Shao's group

The short version of the paper was presented at ICAE2018, Aug 22-25, Hong Kong. This paper is a substantial extension of the short version of the conference paper.

achieved enhanced ORR and OER activities by tailoring the A-site cation deficiency in $LaFeO_3$ perovskite [37]. A plausible explanation is that the introduction of A-site deficiency leads to the perturbation of the valence state for transition metal. In the perovskite oxides, the A-site deficiency would alter B-site element valence, and also increases the number of active sites toward ORR and the oxygen vacancies on the surface [34, 38-41]. Furthermore, substituting various transition metals elements into $LaMnO_3$ perovskites is also an effective way to enhance the electrocatalytic performance. Inspired by the idea, Litao Yan and co-workers developed Ir doped $(La_{0.8}Sr_{0.2})_{0.95}Mn_{0.95}Ir_{0.05}O_3$ nanoparticles with superior bifunctional catalysts in alkaline solution. Co-doped $LaMnO_3$-graphene catalysts and Ni-doped $La_{0.8}Sr_{0.2}Mn_{0.6}Ni_{0.4}O_3$ catalyst were reported to perform better than the pristine ones [42, 43].

$La_{0.8}Sr_{0.2}MnO_3$ has been proposed as one of the best ORR catalysts whose intrinsic ORR activity can be comparable to that of the commercial Pt/C. However, only few studies explore the electrocatalytic activity of $La_{0.8}Sr_{0.2}MnO_3$ perovskite with the A-site deficiency and B-site Fe doping. In this study, we utilized the sol-gel method to prepare the A-site deficient $(La_{0.8}Sr_{0.2})_{1-x}MnO_3$ (x = 0, 0.02, 0.05) and the A-site cation deficient with B-site Fe doped $(La_{0.8}Sr_{0.2})_{0.95}Mn_{0.5}Fe_{0.5}O_3$ perovskite

The short version of the paper was presented at ICAE2018, Aug 22-25, Hong Kong. This paper is a substantial extension of the short version of the conference paper.

oxides, and subsequently studied their ORR and OER catalytic activities. For the former A-site deficient perovskite oxides, $(La_{0.8}Sr_{0.2})_{0.95}MnO_3$ reveals the best bifunctional catalytic activity in the alkaline electrolyte due to the improvement in the surface absorbed oxygen and Mn^{4+} concentration. Partial substitution of Mn by Fe in $(La_{0.8}Sr_{0.2})_{0.95}MnO_3$ can further improve the surface absorbed oxygen concentration and, thus, boost both OER and ORR. In addition to ORR and OER electrocatalytic activity, we further studied the performance of the perovskite samples as cathode catalyst for practical zinc-air battery. The peak power density and the discharge-charge cycling demonstrated the super catalytic activity of $La_{0.8}Sr_{0.2}MnO_3$–based catalyst with A-site deficiency and B-site Fe doping.

2. Experiments

2.1. Material preparation

The perovskite oxide powders were prepared by sol–gel method. Lanthanum nitrate, strontium nitrate, manganese acetate, iron nitrate were dissolved into deionized water. Then, citric acid and glycine were added to the mixed solution. The mole ratio of citric acid: glycine: metal ions mole ratio is 2:1:1. After that, the

The short version of the paper was presented at ICAE2018, Aug 22-25, Hong Kong. This paper is a substantial extension of the short version of the conference paper.

solution was kept stirring in a water bath at 80 ^{o}C until the formation of the gel. Subsequently, the gel was heated in an oven at 250^{o}C and calcined at 700^{o}C for 4 h to get the powder. Here, $(La_{0.8}Sr_{0.2})_{1-x}MnO_3$ (x=0, 0.02, 0.05) and $(La_{0.8}Sr_{0.2})_{0.95}Mn_{0.5}Fe_{0.5}O_3$ are denoted as LSM1, LSM2, LSM3 and LSMF, respectively

2.2 Characterization

The sample crystallinities and phases were analyzed by X-ray diffraction (XRD) (PANalytical X'Pert3 diffractometer) with a Cu Ka radiation source in the range of 2theta from 20^{o} to 80^{o}. The morphology was observed by scanning electron microscopy (SEM) (EVO-MA10 ZEISS) and the elemental distribution was characterized by energy dispersive spectroscopy (EDS) mapping (JEOL JSM 820). The structure was demonstrated by high-resolution transmission electron microscope (HR-TEM) analysis (FEI Tecnai G2 F30). The surface chemical composition of each sample was characterized by a X-ray photoelectron spectroscopy (XPS) system (PHI-5000 Versaprobe) with Mg Kα radiation (hν =1253.6 eV).

2.3 Electrochemical Measurements

The short version of the paper was presented at ICAE2018, Aug 22-25, Hong Kong. This paper is a substantial extension of the short version of the conference paper.

The electrochemical catalytic activities of the samples were measured by rotating disk electrode (RDE) technique (Pine Instruments, Inc.). The RDE is a three-electrode test system that includes a platinum foil (2 cm^2), a saturated Ag/AgCl electrode, and a glassy carbon substrate (0.196 cm^2). The three modules of the system play the role of counter, reference, and working electrodes, respectively. For all of the tests, 0.1 M KOH acts as the electrolyte. Oxide (5 mg) and Vulcan-XC72 carbon (5 mg) were dispersed in 0.9 mL isopropanol solvent mixed with 0.1mL of Nafion (5 wt %, DuPont) solution and then stirring for 1h to get the homogenous ink. To find out the proper loading of the perovskite catalyst, 6μl, 9μl, 12μl, 15μl, 18μl and 24μl of catalyst ink were dropped onto the glass carbon electrode. The loadings of the catalyst were calculated to be 152μg·cm^{-2}, 229μg·cm^{-2}, 305μg·cm^{-2}, 382μg·cm^{-2}, 458 μg·cm^{-2} and 534μg·cm^{-2} respectively. Besides, commercial Pt/C (20 wt%, Aladdin Corp.) was used as the reference catalyst. The loading amount of Pt/C catalyst was 229 μg cm^{-2}. Before the RDE experiments, the setup were purged with pure oxygen gas (99.9%) for 30 min to make the electrolyte saturated with oxygen. The polarization curves were tested in 0.1 M O_2-saturated KOH electrolyte by a CHI electrochemical workstation at scan rate of 10mv/s. ORR was tested at the speeds of 100, 400, 900, and 1600 rpm while OER was tested at 1600 rpm. Electrochemical impedance

The short version of the paper was presented at ICAE2018, Aug 22-25, Hong Kong. This paper is a substantial extension of the short version of the conference paper.

measurements were performed during the frequency between 0.1 Hz and 100 kHz with voltage bias of 5 mV amplitude. The stability of the as prepared catalysts for OER and ORR were executed at 1600 rpm at fixed potentials of -0.4 V (vs. Ag/AgCl) and 0.7 V (vs. Ag/AgCl) for ORR and OER, respectively. All tests were conducted at room temperature (25^{o}C).

2.4 Zinc-Air Battery Fabrication and Evaluation

The zinc-air battery was composed of a zinc plate (0.3 mm thickness) anode, an alkaline electrolyte (6M KOH+0.2M $Zn(Ac)_2$) and an air-cathode. The air cathode consisted of nickle form, with a gas diffusion layer (GDL) (Toray TGP-H-060) on air-facing side and a catalyst layer on the water-facing side. The cathode catalyst was prepared by the following steps. First, 10 mg catalyst and 20 mg activated carbon were first dispersed into 2 ml ethanol. Then, 200 μl of 5 wt % Nafion was added to the mixture and stirring for 2h. After that, the catalyst ink was sprayed onto the nickle form by air-brush coating method. The catalyst loading was estimated to be 2 mg cm^{-2}. The discharge-charge profiles were evaluated in a constant current mode using a battery analyzer (Nenware BTS7.6). Discharge-charge cycling measurements were conducted at a constant current density of 10 mA cm^{-2} with each cycle, which

The short version of the paper was presented at ICAE2018, Aug 22-25, Hong Kong. This paper is a substantial extension of the short version of the conference paper.

included a 5-min discharge step followed by a charge step with the same duration. All experiments were performed at room temperature.

3 Results and discussion

The phase and crystal structure of the as prepared $(La_{0.8}Sr_{0.2})_{1-x}MnO_3$ (x = 0, 0.02, 0.05) and $(La_{0.8}Sr_{0.2})_{0.95}Mn_{0.5}Fe_{0.5}O_3$ perovskite oxides were analyzed by XRD as shown in Fig. 1a. As we can see, after calcined at 700 ^oC for 4 h, all samples can become single phase. The main peaks can be well indexed to cubic structure without any detectable impurities, indicating that neither A-site deficiency nor B-site doping has any influence on the crystalline structure of perovskite. For the A-site cation deficient $(La_{0.8}Sr_{0.2})_{1-x}MnO_3$ (x = 0, 0.02, 0.05) perovskites, the main peaks (110) shift slightly to higher angles with the A-site deficiencies (Fig. 1b). Such a lattice reduction is mainly attributed to the creation of some smaller Mn cations (from 0.645 Å for Mn^{3+} to 0.53 Å for Mn^{4+}). Otherwise, in comparison with LSM3, the main diffraction peak of LSMF moves toward the low angle with the Fe doping. Since LSMF has similar A-site deficiency with LSM3, the observed perturbations of the peak and lattice parameters should be attributed to the larger Fe^{4+} (0.58 Å) ionic radius

The short version of the paper was presented at ICAE2018, Aug 22-25, Hong Kong. This paper is a substantial extension of the short version of the conference paper.

compared with Mn^{4+} (0.53 Å). The result is in good agreement with the XRD Rietveld refinements of the prepared perovskite samples as shown in Fig. 1c-f. All samples exhibit a well-formed cubic symmetrical perovskite structure (Pm-3m). The lattice parameters slightly decrease with the A-site deficiencies (a=b=c=3.8807 Å for LSM1, a=b=c=3.8803 Å for LSM2, a=b=c=3.8800 Å for LSM3), in consistence with the positive shift of XRD peaks. Compared with LSM3, the lattice parameters of LSMF (a=b=c=3.8927 Å) are notably increased. The expanded lattice implies more oxygen vacancy in LSMF than LSM3, which is the key factor to enhance the ORR and OER activities.

The short version of the paper was presented at ICAE2018, Aug 22-25, Hong Kong. This paper is a substantial extension of the short version of the conference paper.

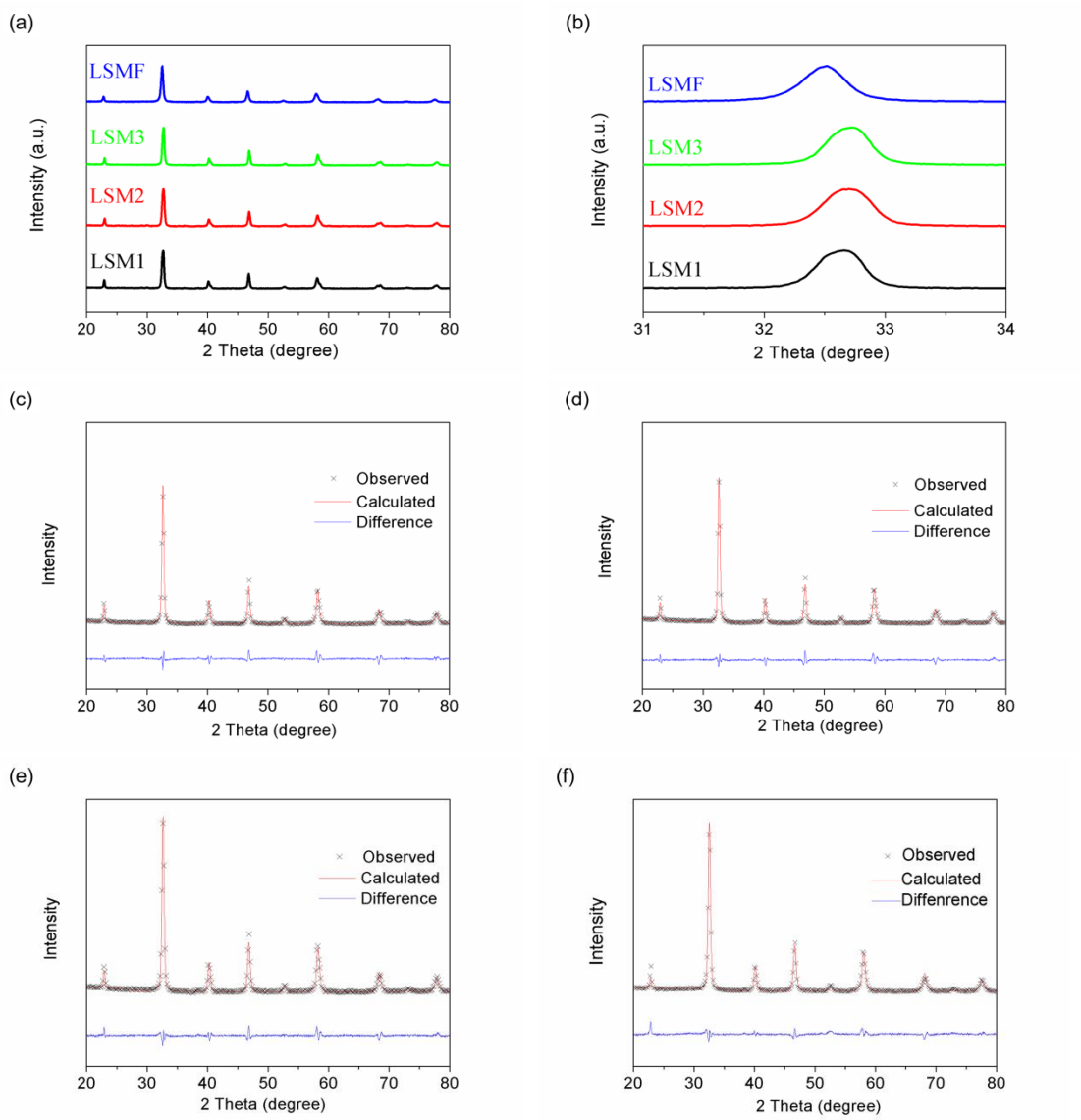

Fig. 1. (a) XRD patterns of $(La_{0.8}Sr_{0.2})_{1-x}MnO_3$ (x = 0, 0.02, 0.05) and $(La_{0.8}Sr_{0.2})_{0.95}Mn_{0.5}Fe_{0.5}O_3$; (b)enlarged XRD patterns at 2θ=31-34°; (c) Refined diffraction patterns of LSM1; (d) Refined diffraction patterns of LSM2; (e) Refined diffraction patterns of LSM3; (f) Refined diffraction patterns of LSMF.

The short version of the paper was presented at ICAE2018, Aug 22-25, Hong Kong. This paper is a substantial extension of the short version of the conference paper.

The surface morphologies of the as-synthesized $La_{0.8}Sr_{0.2})_{1-x}MnO_3$ (x = 0, 0.02, 0.05) and $(La_{0.8}Sr_{0.2})_{0.95}Mn_{0.5}Fe_{0.5}O_3$ perovskite powders were explored by scanning electron microscopy as shown in Fig. 2a-d. Interconnected double- or triple-layer particles with size of hundreds of nanometers are observed in all samples. Besides, the particles exhibit irregular shapes and non-uniform distribution. The particle size decreases (LSM1>LSM2>LSM3) with increase in A-site deficiency. In comparison with LSM3, the B-site iron doped LSMF sample has a slightly larger particle size. The changes in particle sizes may be attributed to the changes in the composition of the perovskites. Figure 2e shows the representative EDS elemental mapping of $(La_{0.8}Sr_{0.2})_{0.95}Mn_{0.5}Fe_{0.5}O_3$ under SEM mode. Each chemical element is uniformly distributed in the perovskite sample. Specially, the uniformly distributed Fe element in the sample indicates that Fe occupies the position of Mn in B-site.

The short version of the paper was presented at ICAE2018, Aug 22-25, Hong Kong. This paper is a substantial extension of the short version of the conference paper.

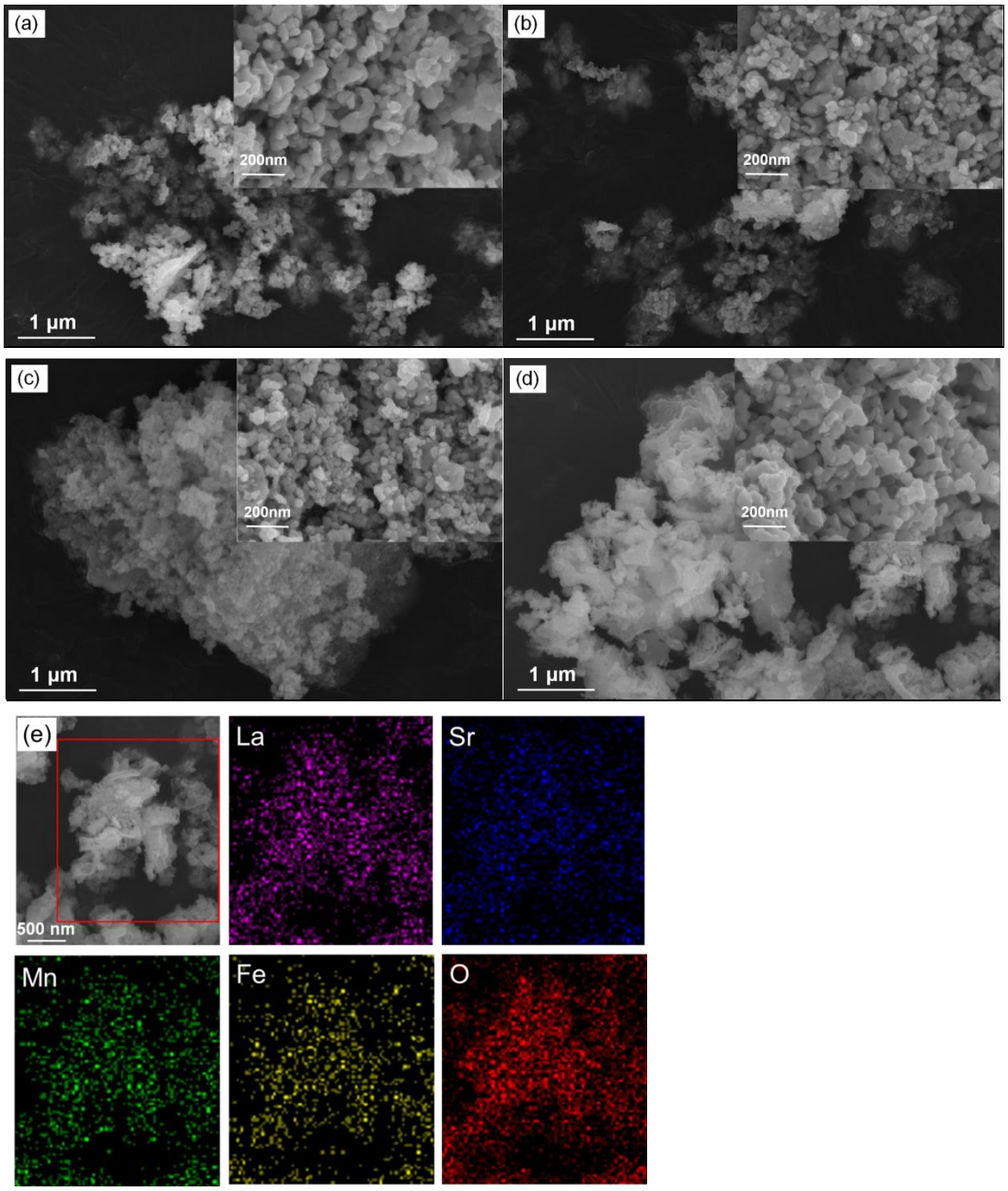

Fig. 2 SEM micrographs of (a) LSM1, (b) LSM2, (c) LSM3 and (d) LSMF (top right insets show the magnified images) (e) EDS elemental mapping of LSMF.

The short version of the paper was presented at ICAE2018, Aug 22-25, Hong Kong. This paper is a substantial extension of the short version of the conference paper.

Figure 3 shows the high-resolution TEM of $(La_{0.8}Sr_{0.2})_{1-x}MnO_3$ (x = 0, 0.02, 0.05) and $(La_{0.8}Sr_{0.2})_{0.95}Mn_{0.5}Fe_{0.5}O_3$ perovskite samples with well-defined lattice fringes. Lattice plane analysis of $(La_{0.8}Sr_{0.2})_{1-x}MnO_3$ (x = 0, 0.02, 0.05) display the interplanar distance of 0.3879 nm, 0.3853 nm, 0.3845 nm, respectively, in good agreement with (100) planes of the cubic ABO_3 perovskite. The gradual decrease in interplanar spacing from LSM1 to LSM3 is in conformity with the positive shifting trend of XRD peaks and calculated lattice parameters. In addition, LSMF exhibits an interplanar distance of 0.3897 nm; the dwelling volume proves the negative shift of XRD peaks. In addition, the fast Fourier transform (FFT) patterns show regular bright spots, indicating well-grown single crystallites of the perovskite samples.

The short version of the paper was presented at ICAE2018, Aug 22-25, Hong Kong. This paper is a substantial extension of the short version of the conference paper.

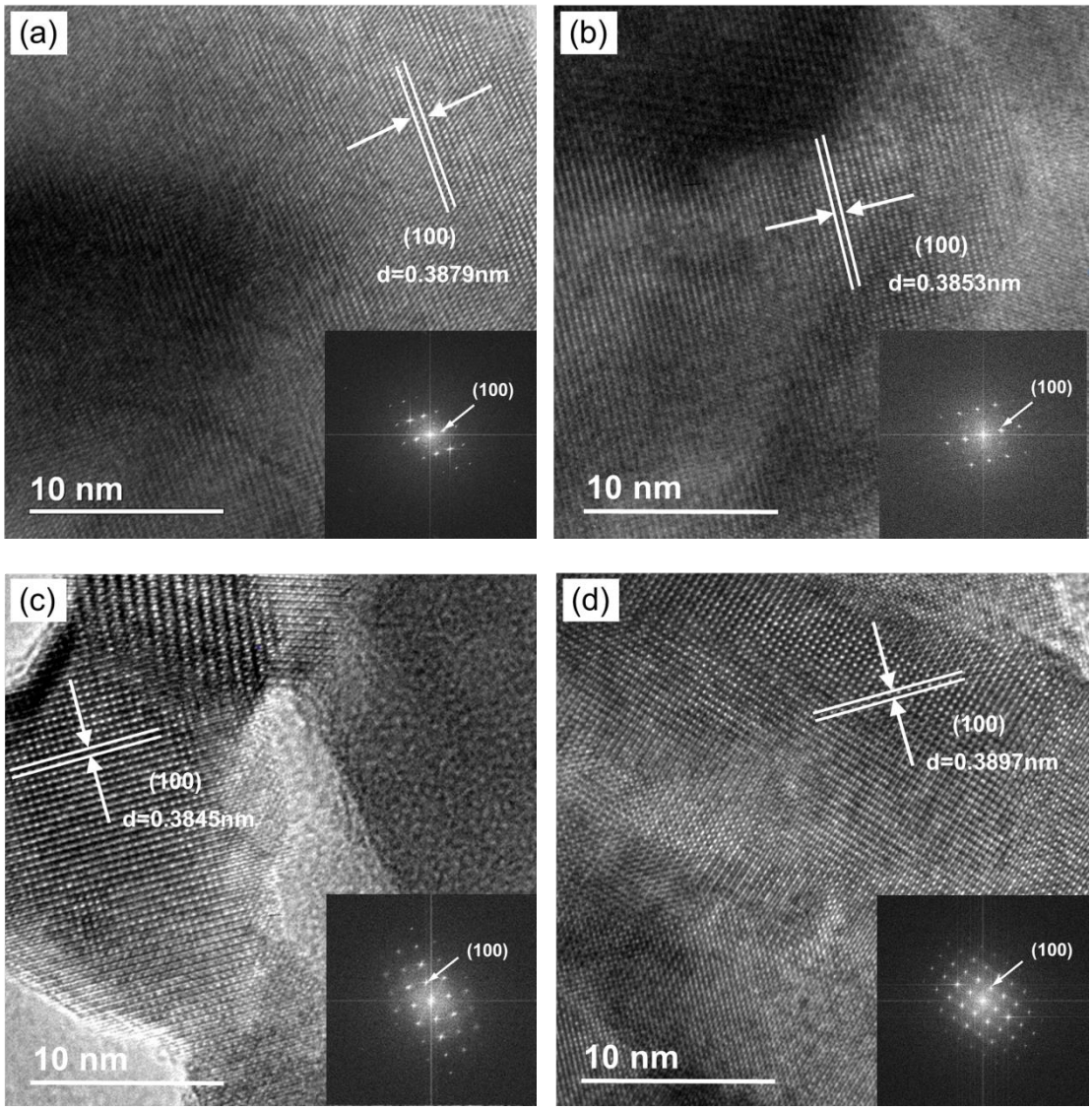

Fig. 3. High-resolution TEM image of (a) LSM1, (b) LSM2, (c) LSM3, (d) LSMF (bottom right insets show the FFT images)

Traditionally, the ORR and OER activities largely depend on the concentration of oxygen vacancy and the valence state of transition metal on the catalysts [44-47]. X-ray photoelectron spectroscopy was performed to obtain the surface chemical composition and the cation oxidation state of the perovskite samples. The O1s

The short version of the paper was presented at ICAE2018, Aug 22-25, Hong Kong. This paper is a substantial extension of the short version of the conference paper.

spectrums of the four catalysts are shown in Fig. 4a. The O1s spectrum is mainly comprised of four types of oxygen species. The lattice oxygen (O_{lat}) is located at ~529.2 eV (O_{ads}). The peaks at the binding energy of 530.5 eV and 531.5 eV are related to highly oxidative oxygen species (O_2^{2-}/O^-) and the surface-adsorbed oxygen/hydroxyl groups (O_2/OH^-), respectively [37, 48, 49]. The peak at 532.8 eV is induced by the surface molecular water or carbonates [50, 51]. The mass percent of the oxygen species which are obtained from the deconvolution of the peaks are summarized in Table 1. As can be seen, the mass percent of O_2^{2-}/O^- species increases in the order of LSM1 < LSM2 < LSM3 < LSMF. As the O_2^{2-}/O^- species is related to the oxygen vacancy, which is the primary ingredient on the surface that is responsible for the electrochemical activity, the slight increase in the A-site stoichiometry is beneficial for bifunctional electrocatalytic activity.

The core-level Mn2p XPS spectra are displayed in Fig. 4b. The peak situated at 642.1 eV can be assigned to Mn 2p1/2. While the Mn 2p3/2 peak which was located at 653.7 eV can be fitted into two peaks at 641.8 and 643 eV, corresponding to Mn^{3+} and Mn^{4+} [52]. The percentages of Mn^{3+} and Mn^{4+} can be calculated from the relative area of the fitted subpeaks (Table 1). The content of Mn^{4+} in LSM1 is 49.8%, and then it further increased to 51.2% for LSM2 and 58.7% for LSM3. The high

The short version of the paper was presented at ICAE2018, Aug 22-25, Hong Kong. This paper is a substantial extension of the short version of the conference paper.

oxidation ability of Mn^{4+} can facilitate the chemical disproportionation of HO_2^- to form O_2, resulting in high OER performance. Otherwise comparing with LSM3, the mass percent of Mn^{4+} in LSMF is decreased, partial replacement of the Mn^{4+} by Fe^{4+}.

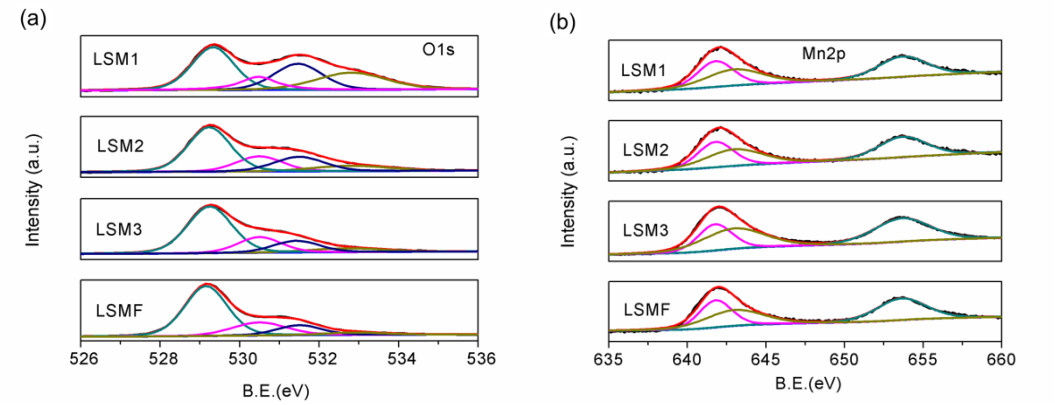

Fig. 4. (a) O1s XPS and (b) Mn2p XPS for LSM1, LSM2, LSM3 and LSMF.

catalyst	H_2O(%)	O_2/OH^-(%)	O_2^{2-}/O^-(%)	O_{Lat}(%)	Mn^{3+}(%)	Mn^{4+}(%)
LSM1	24.8	25.7	12.5	37	50.2	49.8
LSM2	11.5	20.3	18.1	50.1	48.8	51.2
LSM3	7.5	15.3	18.9	58.3	41.3	58.7
LSMF	4.2	13.3	20.7	61.8	48.7	51.3

Table 1 The analyses data of O1s and Mn2p3/2 XPS for LSM1, LSM2, LSM3 and LSMF.

The short version of the paper was presented at ICAE2018, Aug 22-25, Hong Kong. This paper is a substantial extension of the short version of the conference paper.

The effect of catalyst loading was studied with LSM1 catalyst by RDE measurement system at the rotation speed of 1600 rpm in O_2 saturated 0.1 M KOH solution. As shown in Fig. 5, the ORR catalytic activity improves rapidly with increasing catalyst loading when the loading is below 305 μg·cm^{-2} (12 μl). Further increases in the loading of catalyst until 458 μg·cm^{-2} (18 μl), the catalytic activity increases slightly. When the loading reaches 534 μg·cm^{-2} (21 μl), the ORR catalytic activity starts to decrease. This phenomenon is mainly due to the detachment of catalyst layer during the test when the catalyst layer was too thick. For this reason, in the following test, the loading of perovskite catalysts was set to be 458 μg·cm^{-2}.

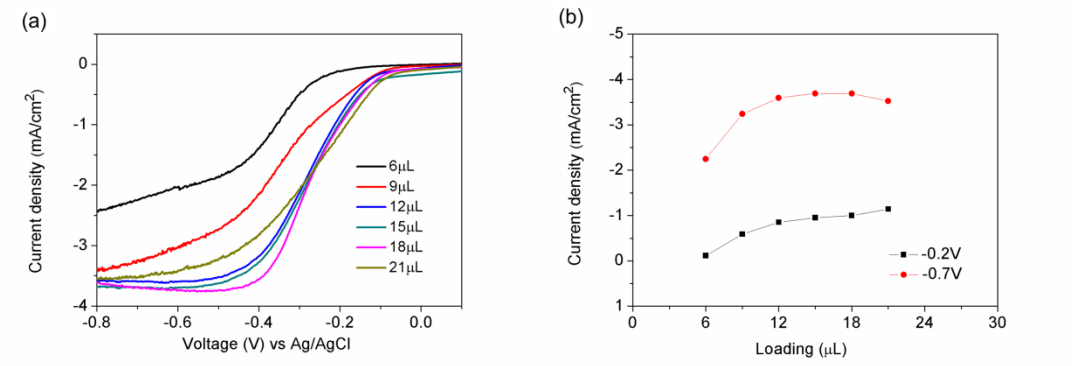

Fig. 5. (a) ORR Linear sweep voltammetry curves of LSM1 catalyst with different loading; (b) Current density at -0.2V and -0.7V vs Ag/AgCl as a function of catalyst loading.

The short version of the paper was presented at ICAE2018, Aug 22-25, Hong Kong. This paper is a substantial extension of the short version of the conference paper.

The ORR and OER catalytic activities of the prepared perovskite samples were evaluated with proper loading in alkaline media. Figure 6a shows the ORR LSV curves for all the perovskite catalysts. In Fig. 6a, the onset potentials (the potential at 0.5 mA cm^{-2}) of the catalyst slightly shift positively with the increase of A-site deficiency. The onset potential of LSM2 with the A-site stoichiometry of 0.98 is -0.14 V vs. Ag/AgCl, which is larger compared with pristine LSM1 (-0.15 V vs. Ag/AgCl) and the data can further increases to -0.134 V vs. Ag/AgCl when the A-site stoichiometry is 0.95. To gain more insights into ORR catalytic activity of the LSM based catalysts, the Tafel curves calculated by the Tafel equation are shown in Fig. 6b.The Tafel slopes for LSM2 and LSM3 are smaller than LSM1, implying higher ORR rates of the former. Besides, we can also conclude that A-site cation deficiency remarkably improve the ORR activity, especially for LSM3. When parts of Mn was substituted by Fe cations in LSM3, the catalytic activity altered, the onset potential shifts more positively to -0.124 V (vs. Ag/AgCl). Among the four samples, LSMF showed the highest current density of about 4.5 mA cm^{-2} which is compatible to Pt/C (5 mA cm^{-2}). The Tafel slope of the LSMF is -137 mV dec^{-1}, which is the lowest among the four samples and close to that of Pt/C (132 mV dec^{-1}). Figures 6c and 6d are the LSV curves of LSM3 and LSMF catalyst measured from 100 rpm to 1600 rpm.

The short version of the paper was presented at ICAE2018, Aug 22-25, Hong Kong. This paper is a substantial extension of the short version of the conference paper.

Obviously, LSMF possesses larger limiting current density at the same speed, showing that Fe-doping benefits the mass transfer between bulk phase electrolyte and electrode surface.

The stability of the electrocatalysts is crucial for the real scenarios. To measure the durability of ORR, chronoamperometric measurements were performed at -0.4 V (vs. Ag/AgCl) at 1600 rpm for 10000 s. As can be seen in Fig. 6e, LSMF shows only a slight degradation after 10000 s, the current retention is 97.1% which is higher than the commercial Pt/C (93.5%).

The short version of the paper was presented at ICAE2018, Aug 22-25, Hong Kong. This paper is a substantial extension of the short version of the conference paper.

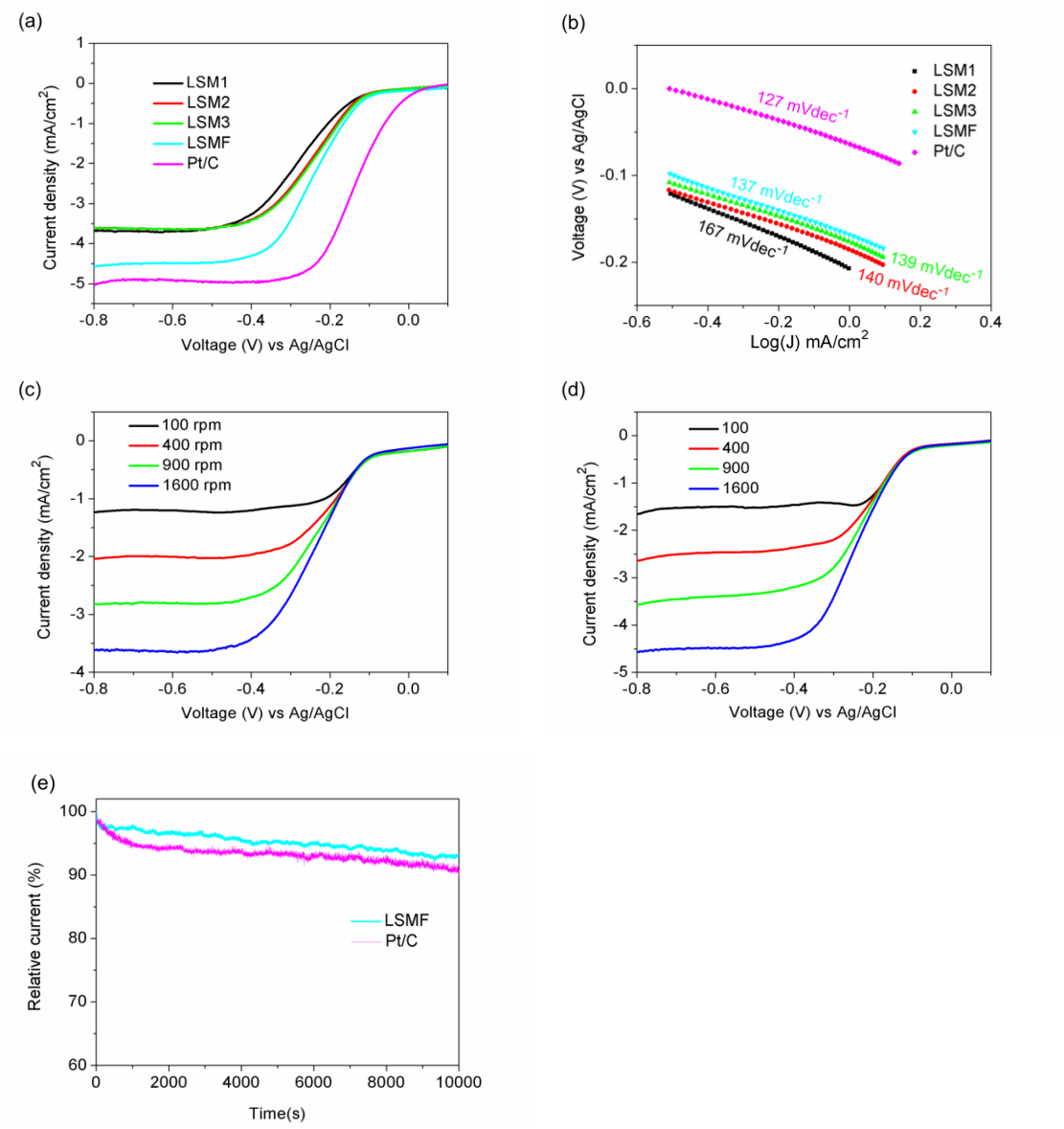

Fig. 6 (a) ORR Linear sweep voltammetry (LSV) curves at 1600 rpm; (b) Corresponding Tafel plots; (c) LSV curves of LSM3 at 100 to 1600 rpm; (d) LSV curves of LSMF at 100 to 1600 rpm; (e) Chronoamperometric response of LSMF and commercial Pt/C at -0.4V vs Ag/AgCl.

The short version of the paper was presented at ICAE2018, Aug 22-25, Hong Kong. This paper is a substantial extension of the short version of the conference paper.

The OER catalytic activities were measured to characterize the potential of the perovskite oxides as bifunctional oxygen electrocatalysts. Fig. 7a shows the LSV curves of the perovskite samples within the potential window. The onset potential (the potential at 0.5 mA cm^{-2}) for LSM2 (~0.6 V vs Ag/AgCl) and LSM3 (~0.57 V vs Ag/AgCl) is much smaller and almost 0.1 V negative shift than that for pristine LSM1 (~0.68 V vs Ag/AgCl), implying that A-site deficient perovskite with more oxygen vacancy exhibits larger current density and thus benefits the OER catalytic activity. For the doped LSMF catalyst, an even much lower onset potential (~0.53 V vs Ag/AgCl) observed demonstrates stronger OER activity than undoped perovskite. Furthermore, Fig. 7b shows the kinetics of the catalysts by the Tafel plots and Fig. 7c shows the electrochemical impedance spectroscopy (EIS) analysis. Since the kinetics is promoted, the OER activity was consequently improved. In Fig. 7b, LSMF showed a smaller Tafel slope, indicating higher OER rates and better charge transfer ability among all the catalysts. Electrode polarization resistance R_P for OER measured at 1 V vs Ag/AgCl on LSMF catalysts was ~96 Ω, substantially smaller than 289 Ω, 215 Ω and 142 Ω measured on LSM1, LSM2 and LSM3 respectively. Note that the order of OER activity for the LSM based catalysts is similar to ORR activity: LSMF>LSM3 >LSM2> LSM1. Nevertheless, the enhanced effect in OER activity is

The short version of the paper was presented at ICAE2018, Aug 22-25, Hong Kong. This paper is a substantial extension of the short version of the conference paper.

higher than ORR activity. Consequently, A-site cation deficiency or B-site Fe doping in LSMF perovskite could largely promote both the ORR activity and the OER activity.

For evaluating the durability, the stability of LSMF and commercial Pt/C was evaluated by the chronoamperometry (CA) measurements at 0.7 V versus Ag/AgCl as shown in Fig. 7d. For a continuous 10000s test, commercial Pt/C lost as much as 84% of its initial activity, while LSFM shows a much higher stability with 35% retention. The results clearly indicate that LSMF is more stable than commercial Pt/C. Furthermore, these also demonstrate the super bifunctionality of introducing A-site cation deficiency and B-site Fe doping in LSMF perovskite.

The short version of the paper was presented at ICAE2018, Aug 22-25, Hong Kong. This paper is a substantial extension of the short version of the conference paper.

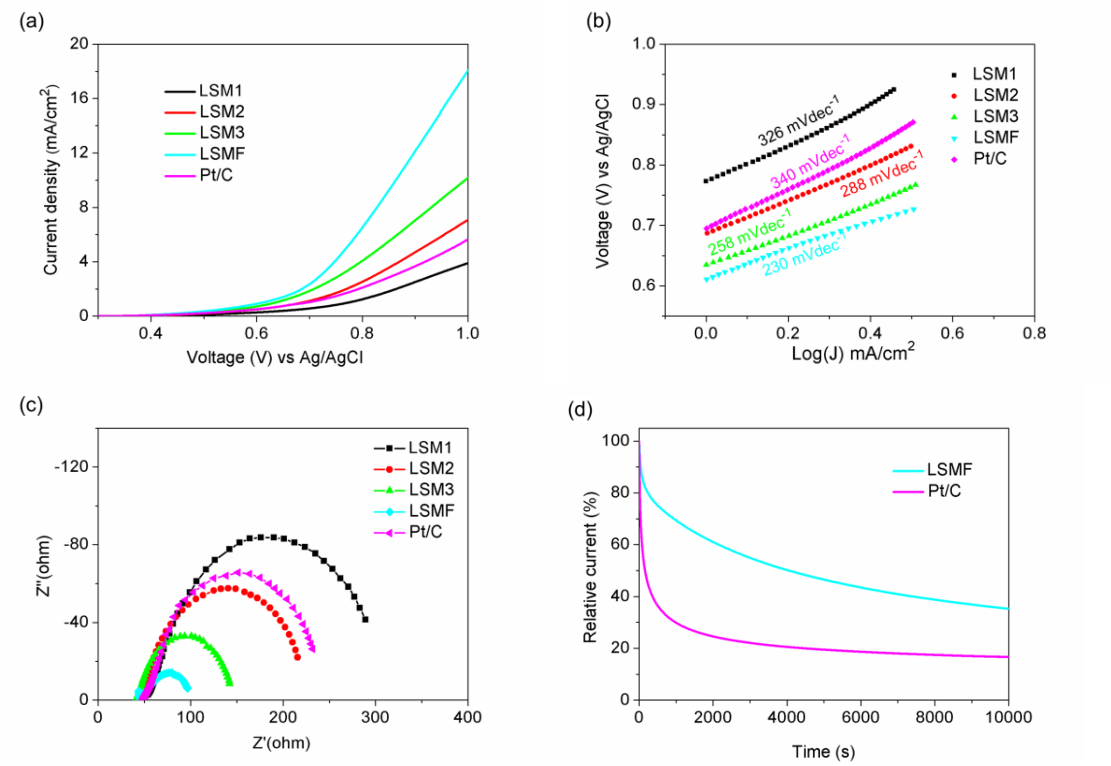

Fig. 7 (a) OER Linear sweep voltammetry (LSV) curves at 1600 rpm; (b) Corresponding Tafel plots; (c) Electrochemical impedance spectroscopy plots at 1.0V vs Ag/AgCl; (d) Chronoamperometric response of LSMF and commercial Pt/C at 0.7V vs Ag/AgCl.

For practical application, zinc-air batteries were assembled with the developed catalysts. Figures 8a shows the I-V-P polarization curves for all the catalysts. For the battery with pristine LSM1 catalyst, the voltage drops quickly with the current density and the peak power density is 73 mW cm^{-2}. Meanwhile, for the batteries using LSM2 and LSM3 catalysts, the peak power densities slightly increase to 79 mW cm^{-2} and 83

The short version of the paper was presented at ICAE2018, Aug 22-25, Hong Kong. This paper is a substantial extension of the short version of the conference paper.

mW cm^{-2}, respectively. For the zinc-air battery using LSMF catalyst, the peak power density significantly increases to 105 mW cm^{-2}, almost 1.5 times higher than that of pristine LSM1. The value is much closer to that of Pt/C (116 mW cm^{-2}). The above results reveal the positive effects of the A-site deficiency and the B-site Fe doping on the catalytic activity of the perovskite. The perovskite catalysts were tested at different current densities of 2, 5 and 10 mA cm^{-2}. As shown in Fig. 8b, the results again prove that LSMF performs with the best catalytic activity among all the perovskite catalysts, in good agreement with the results shown in Figs. 6 and 7. The discharge curves at a current density of 10 mA cm^{-2} are shown in Fig. 8c. It is observed that the zinc-air batteries using LSMF and Pt/C exhibit voltage plateaus of about 1.19V and 1.25V, respectively. With the consumption of zinc plate, the final duration of LSMF was 56300s, much longer than that of Pt/C (53180s). The cycling stability was evaluated by a pulse discharge-charge measurement at a high current density of 10 mA cm^{-2}. As shown in Fig. 8d, LSMF exhibits notably stable discharge-charge voltages for the whole test. The voltage gap for the first cycle is 0.88 V (1.18 V for discharge and 2.06 V for charge). It only increases to 1 V after 100 cycles (The insert picture). For the battery using Pt/C as shown in Fig. 8e, the voltage gap for the first cycle is almost the same with LSMF, but the battery quickly degrades

The short version of the paper was presented at ICAE2018, Aug 22-25, Hong Kong. This paper is a substantial extension of the short version of the conference paper.

and eventually fails at 52nd cycle (discharge voltage drops down to 0.5V). The energy efficiency, defined as the ratio of energy delivered during discharge to the energy consumed during charge, reveals the better stability of LSMF compared with Pt/C (Fig. 8f). The slight decay for LSMF battery is mainly due to the loss of active carbon corrosion during OER and the degradation of zinc plate. Whereas for Pt/C battery, apart from the corrosion of the active carbon support, detachment of Pt particles from carbon support and the agglomeration also lead to the degradation of the battery [53].

The short version of the paper was presented at ICAE2018, Aug 22-25, Hong Kong. This paper is a substantial extension of the short version of the conference paper.

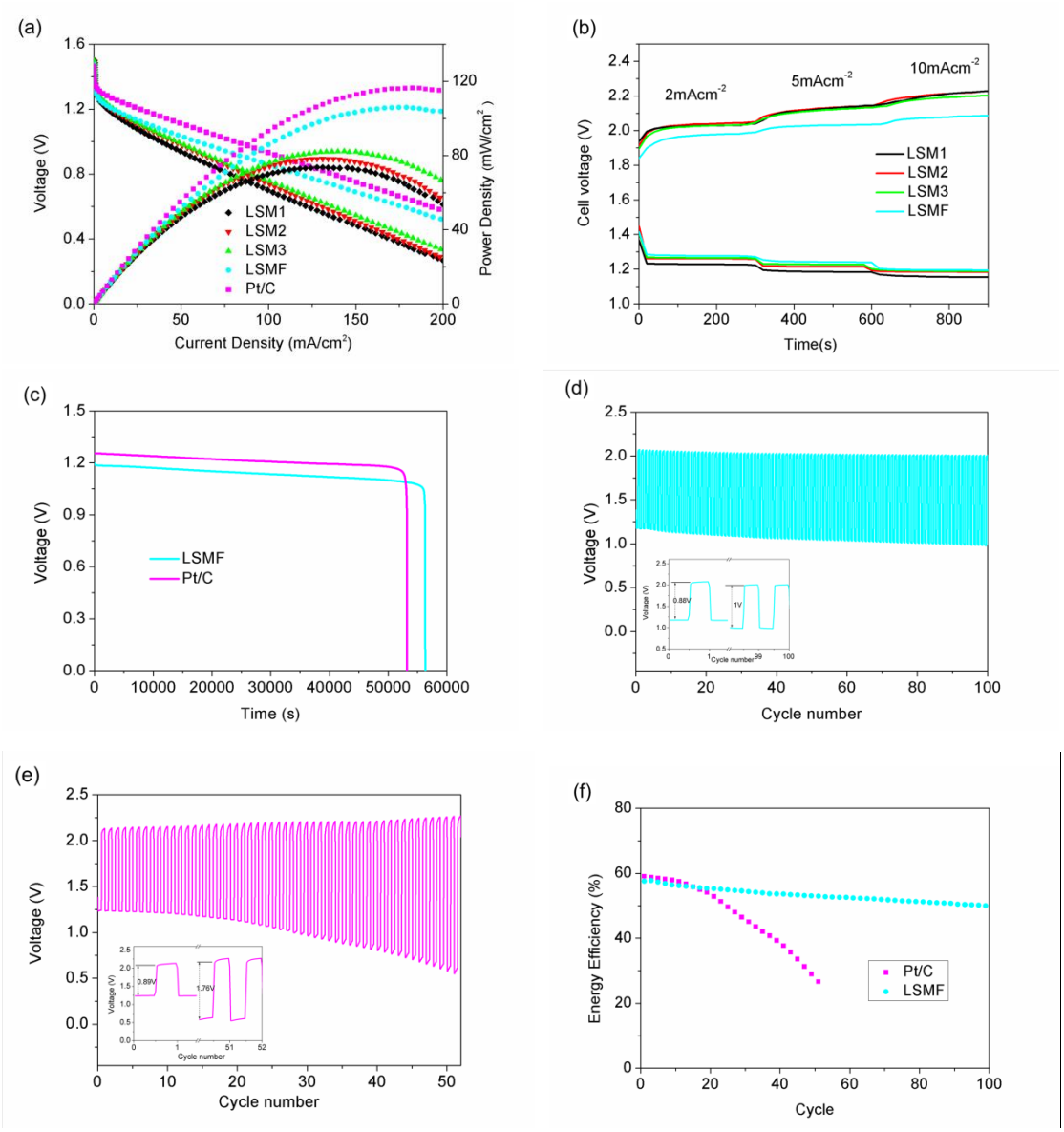

Fig. 8. (a) I-V-P curves; (b) Charge-discharge curves of zinc-air batteries at the current density of 2 mA cm^{-2}, 5 mA cm^{-2} and 10 mA cm^{-2}; (c) Discharge voltage curves of zinc-air batteries at a current density of 10 mA cm^{-2}; (d) Discharge-charge cycling performance of zinc-air battery with LSMF cathode catalyst (The insert is the cycling curves for the selected cycle); (e) Discharge-charge cycling performance of

The short version of the paper was presented at ICAE2018, Aug 22-25, Hong Kong. This paper is a substantial extension of the short version of the conference paper.

zinc-air battery with Pt/C cathode catalyst (The insert is the cycling curves for the selected cycle). (e) Energy efficiency for the whole cycle.

5. Conclusions

In summary, the A-site cation deficient $(La_{0.8}Sr_{0.2})_{1-x}MnO_3$(x=0, 0.02, 0.05) and Fe doped $(La_{0.8}Sr_{0.2})_{0.95}Mn_{0.5}Fe_{0.5}O_3$ perovskites are prepared by sol-gel process. Electrochemical results show that the ORR and OER activities of the samples are controlled by tuning the A-site cation deficiency in $La_{0.8}Sr_{0.2}MnO_3$ perovskite. The electrocatalytic activity is greatly enhanced in the OER procedure. For the A-site cation deficient $(La_{0.8}Sr_{0.2})_{1-x}MnO_3$ perovskites studied, the $(La_{0.8}Sr_{0.2})_{0.95}MnO_3$ shows the highest ORR and OER activities that correspond to the optimal bifunctional catalyst in alkaline solution. When Mn was partially substitute by Fe, the oxygen vacancy is further improved and also the electrochemical performance. The battery test results reveal the high power density, low charge-discharge voltage gap and good stability of $(La_{0.8}Sr_{0.2})_{0.95}Mn_{0.5}Fe_{0.5}O_3$. The LSM-based perovskite with A-site cation deficient and B-site Fe doping holds promise for zinc-air batteries.

Acknowledgements

The short version of the paper was presented at ICAE2018, Aug 22-25, Hong Kong. This paper is a substantial extension of the short version of the conference paper.

This research was financially supported by the National Natural Science Foundation of China (21875200) and CityU Shenzhen Knowledge Innovation Program (Basic Research, JCYJ20160428154632404).

References

[1] Li Q, Cao R, Cho J, Wu G. Nanocarbon Electrocatalysts for Oxygen Reduction in Alkaline Media for Advanced Energy Conversion and Storage. Adv Energy Mater. 2014;4:1301415.

[2] Tahir M, Pan L, Idrees F, Zhang X, Wang L, Zou JJ, Wang ZL. Electrocatalytic oxygen evolution reaction for energy conversion and storage: A comprehensive review. Nano Energy. 2017;37:136-57.

[3] Gu P, Zheng M, Zhao Q, Xiao X, Xue H, Pang H. Rechargeable zinc-air batteries: a promising way to green energy. J Mater Chem A. 2017;5:7651-66.

[4] Chao S, Zhang Y, Wang K, Bai Z, Yang L. Flower-like Ni and N codoped hierarchical porous carbon microspheres with enhanced performance for fuel cell storage. Appl Energ. 2016;175:421-8.

[5] Cao R, Lee JS, Liu M, Cho J. Recent Progress in Non-Precious Catalysts for

Metal-Air Batteries. Adv Energy Mater. 2012;2:816-29.

[6] Lee DU, Xu P, Cano ZP, Kashkooli AG, Park MG, Chen Z. Recent progress and perspectives on bi-functional oxygen electrocatalysts for advanced rechargeable metal-air batteries. J Mater Chem A. 2016;4:7107-34.

[7] Fu G, Cui Z, Chen Y, Xu L, Tang Y, Goodenough JB. Hierarchically mesoporous nickel-iron nitride as a cost-efficient and highly durable electrocatalyst for Zn-air battery. Nano Energy. 2017;39:77-85.

[8] Qian Y, Hu Z, Ge X, Yang S, Peng Y, Kang Z, Liu Z, Lee JY, Zhao D. A metal-free ORR/OER bifunctional electrocatalyst derived from metal-organic frameworks for rechargeable Zn-Air batteries. Carbon. 2017;111:641-50.

[9] Cheng F, Chen J. Metal-air batteries: from oxygen reduction electrochemistry to cathode catalysts. Chem Soc Rev. 2012;41:2172-92.

[10] Pei P, Wang K, Ma Z. Technologies for extending zinc-air battery's cyclelife: A review. Appl Energ. 2014;128:315-24.

[11] Nam G, Park J, Choi M, Oh P, Park S, Kim MG, Park N, Cho J, Lee JS. Carbon-Coated Core-Shell Fe-Cu Nanoparticles as Highly Active and Durable Electrocatalysts for a Zn-Air Battery. Acs Nano. 2015;9:6493-501.

[12] Yang Z, Lin L, Xu A. 2D Nanoporous Fe-N/C Nanosheets as Highly Efficient

Non-Platinum Electrocatalysts for Oxygen Reduction Reaction in Zn-Air Battery. Small. 2016;12:5710-9.

[13] Karim NA, Kamarudin SK. An overview on non-platinum cathode catalysts for direct methanol fuel cell. Appl Energ. 2013;103:212-20.

[14] Yao M, Wang N, Hu W, Komarneni S. Novel hydrothermal electrodeposition to fabricate mesoporous film of $Ni_{0.8}Fe_{0.2}$ nanosheets for high performance oxygen evolution reaction. Appl Catal B-Environ. 2018;233:226-33.

[15] Tang S, Zhou X, Xu N, Bai Z, Qiao J, Zhang J. Template-free synthesis of three-dimensional nanoporous N-doped graphene for high performance fuel cell oxygen reduction reaction in alkaline media. Appl Energ. 2016;175:405-13.

[16] Ma C, Xu N, Qiao J, Jian S, Zhang J. Facile synthesis of $NiCo_2O_4$ nanosphere-carbon nanotubes hybrid as an efficient bifunctional electrocatalyst for rechargeable Zn-air batteries. Int J Hydrogen Energ. 2016;41:9211-8.

[17] Wattiaux A, Grenier JC, Pouchard M, Hagenmuller P. Electrolytic Oxygen Evolution in Alkaline-Medium on $La_{1-X}Sr_xFeO_{3-Y}$ Perovskite-Related Ferrites: Influence of Bulk Properties. J Electrochem Soc. 1987;134:1718-24.

[18] Kahoul A, Hammouche A, Poillerat G, De Doncker RW. Electrocatalytic activity and stability of $La_{1-x}Ca_xCoO_3$ perovskite-type oxides in alkaline medium. Catal Today.

2004;89:287-91.

[19] Xu N, Qiao J, Zhang X, Ma C, Jian S, Liu Y, Pei P. Morphology controlled $La_2O_3/Co_3O_4/MnO_2$-CNTs hybrid nanocomposites with durable bi-functional air electrode in high-performance zinc-air energy storage. Appl Energ. 2016;175:495-504.

[20] Zhu Y, Zhou W, Chen Z, Chen Y, Su C, Tadé MO, Shao Z. $SrNb_{0.1}Co_{0.7}Fe_{0.2}O_{3-delta}$ Perovskite as a Next-Generation Electrocatalyst for Oxygen Evolution in Alkaline Solution. Angew Chem Int Edit. 2015;54:3897-901.

[21] Suntivich J, Gasteiger HA, Yabuuchi N, Nakanishi H, Goodenough JB, Shao-Horn Y. Design principles for oxygen-reduction activity on perovskite oxide catalysts for fuel cells and metal-air batteries. Nat Chem. 2011;3:546-550.

[22] Takeguchi T, Yamanaka T, Takahashi H, Watanabe H, Kuroki T, Nakanishi H, Orikasa Y, Uchimoto Y, Takano H, Ohguri N, Matsuda M. Layered Perovskite Oxide: A Reversible Air Electrode for Oxygen Evolution/Reduction in Rechargeable Metal-Air Batteries. J Am Chem Soc. 2013;135:11125-30.

[23] Elumeeva K, Masa J, Sierau J, Tietz F, Muhler M, Schuhmann W. Perovskite-based bifunctional electrocatalysts for oxygen evolution and oxygen reduction in alkaline electrolytes. Electrochim Acta. 2016;208:25-32.

The short version of the paper was presented at ICAE2018, Aug 22-25, Hong Kong. This paper is a substantial extension of the short version of the conference paper.

[24] Hayashi M, Hyodo T, Miura N, Yamazoe N. Electrochemical oxygen reduction properties of perovskite-type oxides $La_{1-x}A_xMnO_3$ (A = Na, K, Rb) in concentrated alkaline solution. Electrochemistry. 2000;68:112-8.

[25] Wei L, Sun L, Li Q, Huo L, Zhao H. Doping Effect of Alkaline Earth Metal on Oxygen Reduction Reaction in Praseodymium Nickelate With Layered Perovskite Structure. J Electrochem Energy. 2016;13:041003

[26] Wang C, Cheng Y, Ianni E, Jiang S, Lin B. A highly active and stable $La_{0.5}Sr_{0.5}Ni_{0.4}Fe_{0.6}O_{3-delta}$ perovskite electrocatalyst for oxygen evolution reaction in alkaline media. Electrochim Acta. 2017;246:997-1003.

[27] Zhuang S, Liu S, Huang C, Tu F, Zhang J, Li Y. Electrocatalytic Activity of Nanoporous Perovskite $La_{1-x}Ca_xCoO_3$ Towards Hydrogen Peroxide Reduction in Alkaline Medium. Int J Electrochem Sc. 2012;7:338-44.

[28] Armstrong EN, Striker T, Ramaswamy V, Ruud JA, Wachsman ED. NO_x adsorption behavior of $LaFeO_3$ and $LaMnO_{3+delta}$ and its influence on potentiometric sensor response. Sensor Actuat B-Chem. 2011;158:159-70.

[29] Ashok A, Kumar A, Bhosale RR, Almomani F, Malik SS, Suslov S, Tarlochan F. Combustion synthesis of bifunctional $LaMO_3$ (M = Cr, Mn, Fe, Co, Ni) perovskites for oxygen reduction and oxygen evolution reaction in alkaline media. J Electroanal

The short version of the paper was presented at ICAE2018, Aug 22-25, Hong Kong. This paper is a substantial extension of the short version of the conference paper.

Chem. 2018;809:22-30.

[30] Bidrawn F, Kim G, Aramrueang N, Vohs JM, Gorte RJ. Dopants to enhance SOFC cathodes based on Sr-doped $LaFeO_3$ and $LaMnO_3$. J Power Sources. 2010;195:720-8.

[31] Kuai L, Kan E, Cao W, Huttula M, Ollikkala S, Ahopelto T, Honkanen AP, Huotari S, Wang W, Geng B. Mesoporous $LaMnO_{3+delta}$ perovskite from spray - pyrolysis with superior performance for oxygen reduction reaction and Zn - air battery. Nano Energy. 2018;43:81-90.

[32] Zhao Y, Hang Y, Zhang Y, Wang Z, Yao Y, He X, Zhang C, Zhang D. Strontium-doped perovskite oxide $La_{1-x}Sr_xMnO_3$ (x=0, 0.2, 0.6) as a highly efficient electrocatalyst for nonaqueous Li-O_2 batteries. Electrochim Acta. 2017;232:296-302.

[33] Hu J, Wang L, Shi L, Huang H. Preparation of $La_{1-x}Ca_xMnO_3$ perovskite-graphene composites as oxygen reduction reaction electrocatalyst in alkaline medium. J Power Sources. 2014;269:144-51.

[34] Konysheva EY, Xu X, Irvine JTS. On the Existence of A-Site Deficiency in Perovskites and Its Relation to the Electrochemical Performance. Adv Mater. 2012;24:528-32.

[35] Hansen KK. The effect of A-site deficiency on the performance of

$La_{1-s}Fe_{0.4}Ni_{0.6}O_{3-delta}$ cathodes. Mater Res Bull. 2010;45:197-9.

[36] Tsai CC, Chu SY, Hong CS, Yang SL. Influence of A-site deficiency on oxygen-vacancy-related dielectric relaxation, electrical and temperature stability properties of CuO-doped NKN-based piezoelectric ceramics. Ceram Int. 2013;39:S165-S70.

[37] Zhu Y, Zhou W, Yu J, Chen Y, Liu M, Shao Z. Enhancing Electrocatalytic Activity of Perovskite Oxides by Tuning Cation Deficiency for Oxygen Reduction and Evolution Reactions. Chem Mater. 2016;28:1691-7.

[38] Kostogloudis GC, Ftikos C. Properties of A-site-deficient $La_{0.6}Sr_{0.4}Co_{0.2}Fe_{0.8}O_{3-delta}$-based perovskite oxides. Solid State Ionics. 1999;126:143-51.

[39] Mineshige A, Izutsu J, Nakamura M, Nigaki K, Abe J, Kobune M, Fujii S, Yazawa T. Introduction of A-site deficiency into $La_{0.6}Sr_{0.4}Co_{0.2}Fe_{0.8}O_{3-delta}$ and its effect on structure and conductivity. Solid State Ionics. 2005;176:1145-9.

[40] Li X, Zhao H, Zhou X, Xu N, Xie Z, Chen N. Electrical conductivity and structural stability of La-doped $SrTiO_3$ with A-site deficiency as anode materials for solid oxide fuel cells. Int J Hydrogen Energ. 2010;35:7913-8.

[41] Xue Y, Miao H, Sun S, Wang Q, Li S, Liu Z. $(La_{1-x}Sr_x)_{0.98}MnO_3$ perovskite with

A-site deficiencies toward oxygen reduction reaction in aluminum-air batteries. J Power Sources. 2017;342:192-201.

[42] Hu J, Wang L, Shi L, Huang H. Oxygen reduction reaction activity of $LaMn_{1-x}Co_xO_3$-graphene nanocomposite for zinc-air battery. Electrochim Acta. 2015;161:115-23.

[43] Wang Z, You Y, Yuan J, Yin Y, Li Y, Xin S, Zhang D. Nickel-Doped $La_{0.8}Sr_{0.2}Mn_{1-x}Ni_xO_3$ Nanoparticles Containing Abundant Oxygen Vacancies as an Optimized Bifunctional Catalyst for Oxygen Cathode in Rechargeable Lithium-Air Batteries. Acs Appl Mater Inter. 2016;8:6520-8.

[44] Suntivich J, Gasteiger HA, Yabuuchi N, Nakanishi H, Goodenough JB, Shao-Horn Y. Design principles for oxygen-reduction activity on perovskite oxide catalysts for fuel cells and metal-air batteries. Nat Chem. 2011;3:546-50.

[45] Yan L, Lin Y, Yu X, Xu W, Salas T, Smallidge H, Zhou M, Luo H. $La_{0.8}Sr_{0.2}MnO_3$-Based Perovskite Nanoparticles with the A-Site Deficiency as High Performance Bifunctional Oxygen Catalyst in Alkaline Solution. Acs Appl Mater Inter. 2017;9:23820-7.

[46] Tulloch J, Donne SW. Activity of perovskite $La_{1-x}Sr_xMnO_3$ catalysts towards oxygen reduction in alkaline electrolytes. J Power Sources. 2009;188:359-66.

The short version of the paper was presented at ICAE2018, Aug 22-25, Hong Kong. This paper is a substantial extension of the short version of the conference paper.

[47] Wu Z, Sun L, Xia T, Huo L, Zhao H, Rougier A, Grenier JC. Effect of Sr doping on the electrochemical properties of bi-functional oxygen electrode $PrBa_{1-x}Sr_xCo_2O_{5+delta}$. J Power Sources. 2016;334:86-93.

[48] Li Z, Lv L, Wang J, Ao X, Ruan Y, Zha D, Hong G, Wu Q, Lan Y, Wang C, Jiang J. Engineering phosphorus-doped $LaFeO_{3-\delta}$ perovskite oxide as robust bifunctional oxygen electrocatalysts in alkaline solutions. Nano Energy. 2018;47:199-209.

[49] She S, Yu J, Tang W, Zhu Y, Chen Y, Sunarso J, Zhou W, Shao Z. Systematic Study of Oxygen Evolution Activity and Stability on $La_{1-x}Sr_xFeO_{3-delta}$ Perovskite Electrocatalysts in Alkaline Media. Acs Appl Mater Inter. 2018;10:11715-21.

[50] Liu R, Liang F, Zhou W, Yang Y, Zhu Z. Calcium-doped lanthanum nickelate layered perovskite and nickel oxide nano-hybrid for highly efficient water oxidation. Nano Energy. 2015;12:115–22.

[51] Zhu Y, Zhou W, Sunarso J, Zhong Y, Shao Z. Phosphorus-Doped Perovskite Oxide as Highly Efficient Water Oxidation Electrocatalyst in Alkaline Solution. Adv Funct Mater. 2016;26:5862–72.

[52] Sun N, Liu H, Yu Z, Zheng Z, Shao C. Mn-doped $La_{0.6}Sr_{0.4}CoO_3$ perovskite catalysts with enhanced performances for non-aqueous electrolyte Li–O_2

batteries. RSC Adv. 2016;6:13522–30.

[53] Peng SJ, Han XP, Li LL, Chou SL, Ji DX, Huang HJ, Du YH, Liu J, Ramakrishna S. Electronic and Defective Engineering of Electrospun $CaMnO_3$ Nanotubes for Enhanced Oxygen Electrocatalysis in Rechargeable Zinc-Air Batteries. Adv Energy Mater. 2018;8:1800612

.

The short version of the paper was presented at ICAE2018, Aug 22-25, Hong Kong. This paper is a substantial extension of the short version of the conference paper.